Research Article | Vol. 13, No. 12 / 1 Dec 2022 / Biomedical Optics Express 6300
Biomedical Optics EXPRESS

Detection of fluorescence-labeled DNA with in-plane organic optoelectronic devices

IGOR TITOV,[1,*] NILS RUTSCHKE,[2] FABIO A. KRAFT,[1] MARKUS KÖPKE,[1] ERIC NEBLING,[3] AND MARTINA GERKEN[1]

[1] *Integrated Systems and Photonics, Faculty of Engineering, Kiel University, Germany*
[2] *altona Diagnostics GmbH, Hamburg, Germany*
[3] *Battery Systems for Special Applications, Fraunhofer Institute for Silicon Technology, Germany*
[*] *igti@tf.uni-kiel.de*

Abstract: We present a system efficiency analysis of a monolithic integrated organic optoelectronic unit for the detection of fluorescence labeled single-stranded DNA (ssDNA) for veterinary disease testing. The side-by-side integration of an organic light emitting diode (OLED) and an organic photodetector (OPD) with 0.5 mm by 0.5 mm device sizes has the potential to enable compact and low-cost fluorescence point-of-care (POC) devices for decentral multiplex biomedical testing. Here, we used two 6-FAM and BHQ1 labeled complementary ssDNA strands to form the Förster resonance transfer (FRET) upon the hybridization of the DNA. In this work we successfully show ssDNA hybridization sensing with samples diluted in TE buffer and investigate the detection of covalently bound 6-FAM-ssDNA on a glass surface for multiplex biomarker measurements.

1. Introduction

Equid herpesviruses (EHV) cause different diseases in equine population and have been reported in five variants named EHV-1 to 5. EHV-1 is the most pathogenic variant and is responsible for neurological and respiratory diseases, abortions as well as equine herpesvirus myeloencephalopathy (EHM) [1]. These severe equine diseases are often followed by loss of life, the inability to move horses and participate in equine races or competitions. Since the virus is transmitted by nose-to-nose contact or by fomites, it is essential to immediately separate the horses and establish quarantine to prevent closure of equine venues or equestrian farms as a consequence [2]. Both result in considerable economic cost to the owner and horse industry and require surveillance and prophylaxis. Thus, the detection of EHV is crucial and a variety of techniques have been reported for the diagnosis. Viral load can be collected in nasal swabs by using viral transport media for further quantification. The confirmation of viral identity can be realized by immunostaining or polymerase chain reaction (PCR) analysis after a virus isolation. Additionally, a nested PCR-enzyme-linked immunosorbent assay (ELISA) has also been reported to detect EHV infection. However, the stated detection techniques suffer from severe disadvantages: they are lab intensive and highly time consuming [3,4]. To overcome the aforementioned limitations lab-on-chip (LOC) systems for rapid point-of-care (POC) diagnosis are of high interest.

The current research aim is to develop a low-cost, widely available and simple to fabricate LOC biosensor for decentral EHV testing. The hybrid integration of organic light emitting diodes (OLEDs) and organic photodetectors (OPDs) promises great potential for highly integrated biosensors. Early work has achieved highly interesting results with the application of OLEDs and OPDs as wearable sensors for pulse oximetry or health monitoring [5–8] and several analytical applications [9,10] fabricated on flexible and rigid substrates. Mayr et al. [11], Pais et al. [12] and Liu et al. [13] presented fluorescence measurement systems based on the hybrid integration of OLEDs and OPDs. Recently Lian et al. [14] published very impressive results utilizing a microcavity OLED for detection of single-stranded DNA (ssDNA) of fetal bovine serum (FBS)

#475358 https://doi.org/10.1364/BOE.475358
Journal © 2022 Received 21 Sep 2022; revised 25 Oct 2022; accepted 26 Oct 2022; published 8 Nov 2022

Biomedical Optics EXPRESS

diluted in phosphate-buffered saline (PBS). Two complementary ssDNA labeled with Cyanine dyes were used to form a Förster resonance energy transfer (FRET) upon the hybridization of the ssDNA to double-stranded DNA (dsDNA). They excited the Cy3-dye with the OLED and detected the fluorescence of the Cy5-dye with an inorganic photodiode, achieving a low limit of detection (LOD) as 1 nM.

While the aforementioned reports are highly relevant, they are not easily upscaled for parallel fabrication of many sensor units. The sensing units are mostly fabricated on separate substrates with one type of optoelectronic device on it. The subsequent lamination to a single unit is liable to misalignment and thus not easy to upscale. To overcome this limitation we aim to develop a monolithic integrated OLED-OPD unit for biosensing applications. Integrating the optoelectronic detection unit on a single substrate is an essential step for ease of alignment and contacting and for the integration with a microfluidic system. Recently we demonstrated the fabrication of OLEDs and OPDs on one single flexible substrate in a matrix integration approach [15] and proposed recently 8 monolithic integrated OLED-OPD pairs with each device size of 0.5 mm * 0.5 mm for point-of-need (PON) nitrite sensing [16]. These detection units are based on thermal evaporation (PVD) device fabrication technique allowing a high degree of miniaturization and permanently aligned optical elements. On the longer term, the fabrication on flexible substrates is highly promising for roll-to-roll fabrication promising a new level of scalability and cost reduction [17,18]. In this work, we adapt the OLED stack for efficient excitation of the fluorophore 6-Carboxyfluorescein (6-FAM). This is a common label for biosensing. We investigate the light budget and efficiency for systems using OLEDs and OPDs integrated on a single substrate in a side-by-side configuration for the detection of fluorescence-labeled ssDNA. We present detection scenarios of fluorescence-labeled ssDNA with a filter-free design of a monolithic integrated OLED-OPD unit shown in the schematic of Fig. 1.

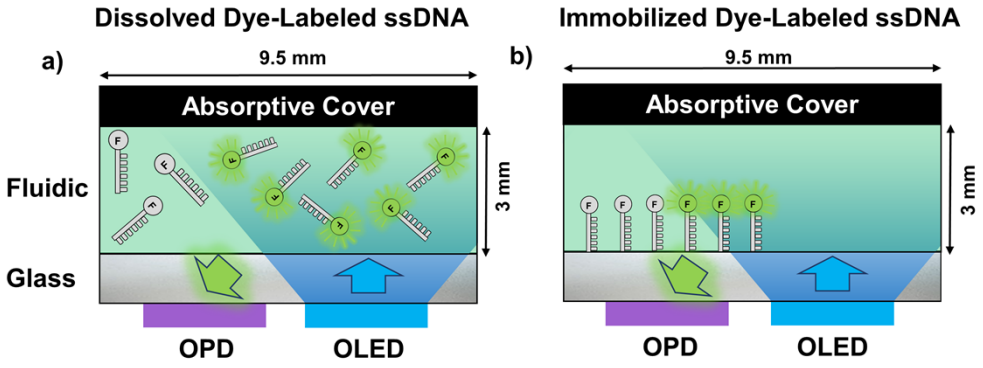

Fig. 1. Schematic view of the analyzed sensing scenarios with the investigated monolithic integrated OLED-OPD unit for detection of fluorescence dye-labeled ssDNA; (a) Sensing of dissolved fluorescence dye-labeled ssDNA in a buffer solution. The fluid chamber contains approx. 270 µl analyte with a certain concentration of dye-labeled ssDNA; (b) Sensing of surface bound dye-labeled ssDNA on a glass substrate.

In the first detection scenario we investigate the sensitivity of sensing fluorescence-labeled ssDNA free diffusive in TE buffer (Fig. 1(a)). The OLED excites the dissolved randomly-orientated fluorescence molecules in a liquid chamber with a volume of approx. 270 µl. The top of the fluidic is covered with a black absorptive polymer cover, to avoid light scattering directly from the OLED to the OPD. We discussed the suppression of stray light using black microfluidic chambers in our previous work [15]. Secondly, we investigate a detection setup with surface bound dye-labeled ssDNA utilized as capture molecules (Fig. 1(b)). Here, we developed a specific ssDNA assay based on the fluorescence quenching mechanism. We covalently coupled

Biomedical Optics EXPRESS

a fluorescence-labeled ssDNA on a glass surface, which is intended to act as a capture molecule. The detection principal bases on the hybridization of the fluorescence-labeled ssDNA strand and a quencher-labeled reverse complementary ssDNA segments, where the fluorescence of the fluorophore is suppressed upon a certain proximity to the quencher [19,20]. After the hybridization of the ssDNA segments to dsDNA the fluorophores undergo FRET. This setup is highly relevant for multiplex measurements. For testing of several specific biomarkers of interest, capture ssDNA can be labeled with different fluorescence molecules. This results in a specific wavelength for certain biomarker, which can be excited and detected with a suitable OLED-OPD pair.

The paper is structured as follows. In section 2 we present the synthesis and the detection principal of the fluorescence-labeled ssDNA and the fabrication and characterization of the OLED-OPD detection unit. Section 3 describes our results with three different measurement setups. Firstly, we show a successful fluorescence quenching of surface bound fluorescence-labeled ssDNA on a fluorescence microscope. Secondly, we show a compact measurement system containing a laser diode as the excitation source and an OPD as the detector. Here we obtained an LOD of 63 µg/l (150 nM) for fluorescein in water and performed successfully DNA hybridization detection. Next, we show the detection of fluorescence-labeled ssDNA on a compact, monolithic integrated OLED-OPD unit with an LOD performance of 0.7 mg/l (1.7 µM) for fluorescein in water. Finally, we give an estimation of the system efficiency by performing ray tracing simulations and verify the theoretical results with experimental measurements. Conclusions are given in section 4.

2. Experimental section

2.1. Chemicals and materials

Following materials were used as the organic components of the devices: 1,1-bis[(di-4-tolylamino)phenyl]cyclohexane (TAPC, CAS-No: 58473-78-2, Merck KGaA, Darmstadt, Germany), tris(4-carbazoyl-9-ylphenyl)amine (TCTA, CAS-No: 139092-78-7, Merck KGaA, Darmstadt, Germany), 2,2',2''-(1,3,5-Benzinetriyl)-tris(1-phenyl-1-H-benzimidazole) (TPBi, CAS-No: 192198-85-9, Luminescence Technology Corp., New Taipei City, Taiwan), Bis[2-(4,6-difluorophenyl)pyridinato-C2,N](picolinato)iridium (FIrPic, CAS-No: 376367-93-0, Ossila Ltd, Solpro Business Park, Windsor Street, Sheffield S4 7WB, U.K.), N,N-Dimethyl quinacridone (DMQA, CAS-No: 19205-19-7, Lumtec), 3',4'-Dibutyl-5,5''-bis(dicyanovinyl)-2,2':5',2''-terthiophene (DCV3T, CAS-No: 908588-68-1, Luminescence Technology Corp., New Taipei City, Taiwan), molybdenum trioxide (MoO_3, CAS-No: 1313-27-5, Merck KGaA, Darmstadt, Germany), lithium fluoride (LiF, CAS-No: 7789-24-4, Merck KGaA, Darmstadt, Germany), aluminum (Al, CAS-No: 7429-90-5, Merck KGaA, Darmstadt, Germany).

2.2. Synthesis of ssDNA for hybridization sensing

The chemical synthesis of modified ssDNA was done using the phosphoramidite method on a solid phase. The nucleotides were added in a cyclic process to the start nucleotide or 3' modification which were bound to a solid phase consisting of Controlled Pore Glass (CPG). During the process, the functionalized groups of phosphates, desoxyribose and nucleobases needed to be temporarily or permanent encapsulated to avoid unwanted side reactions. In the final stage of oligonucleotide synthesis, the oligonucleotide was cleaved from the CPG. The cycle is displayed in Fig. 2.

The synthesis was executed on a DNA/RNA Synthesizer ABI 3900 (Biolytic Lab Performance, Inc., Fremont, USA). The purification of the target ssDNA was carried out by a Reversed Phase Ion Pairing Chromatography (Chromaster, Hitachi High-Tech, Tokio, Japan) in combination with a fractionator (Foxy R2, TELEDYNE ISCO, Inc., Lincoln, USA) according to the hydrophobicity

Biomedical Optics EXPRESS

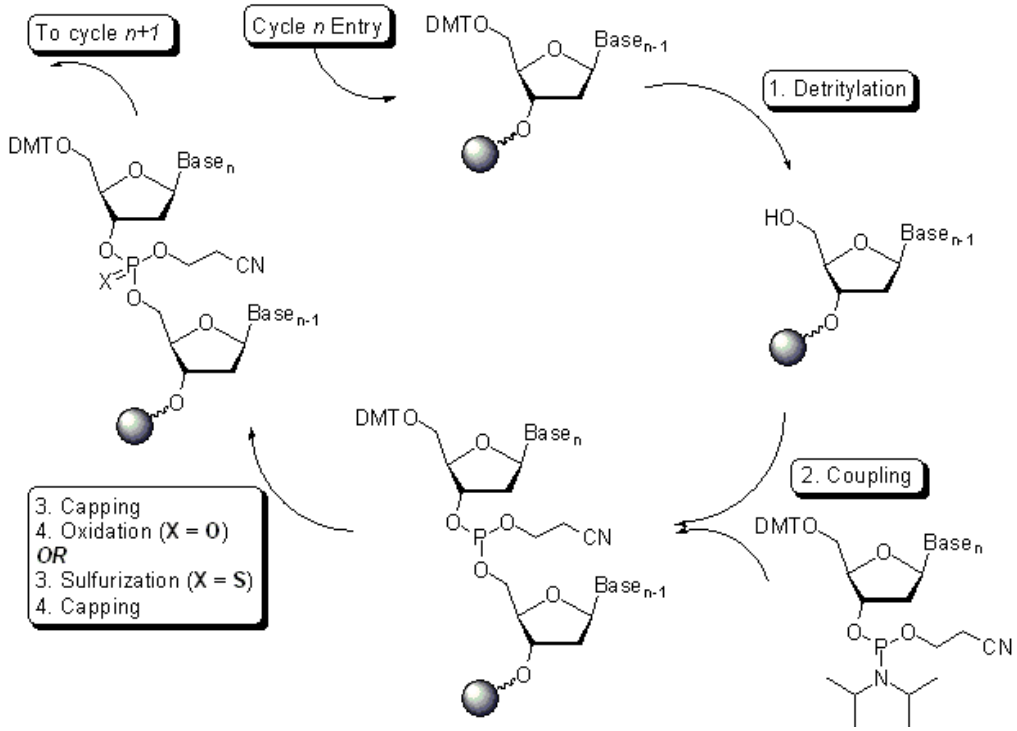

Fig. 2. The phosphoramidite ssDNA synthesis cycle.

and ionic character [21]. The dye-labeled ssDNA sequences were synthesized at altona Diagnostics GmbH and obtained with an initial concentration of 100 µM in TE-buffer.

2.3. Detection principle of 6-FAM-labeled ssDNA

This section focuses on the fluorescence detection principle, after an isothermal amplification reaction. For the target sequence two primers are used, one of the primers is modified with an internal black hole quencher (BHQ1) and a secondary structure. This secondary structure should prevent false positive results and is only unwound when the target sequence is present and amplified (Fig. 3). In case of a successful amplification, the double stranded amplicon is generated with a short single stranded (ss)DNA tail (Fig. 3). This DNA tail is designed to fit to a single stranded reverse complementary capture molecule in another compartment of chip.

For further immobilization of capture molecules we functionalized a glass surface with 3-aminopropyltriethoxysilane (APTES) and modified the amino-silane groups by subsequent adding of *bis*-NHS-PEG compounds. This procedure leads to a crosslinker with homobifunctional NHS-ester compounds for protein interactions [22]. In Fig. 4(a) schematic representations of the APTES and *bis*-NHS-PEG_5 surface functionalization are shown with a verification photograph of a spot (Fig. 4(b)) after successful immobilized fluorescence-labeled ssDNA, visualized on a fluorescence microscope (Leica DMi8, Leica Microsystems CMS GmbH, Wetzlar, Germany).

The capture molecule is immobilized on a glass surface via an amine group at its 5'-End. At the 3'-End the fluorophore 6-Carboxyfluorescein (6-FAM) is orientated (Fig. 5(a)). The detection principal bases on the Förster resonance energy transfer (FRET), where the fluorescence of the fluorophore is suppressed when it is in a certain proximity to the quencher.

Biomedical Optics EXPRESS

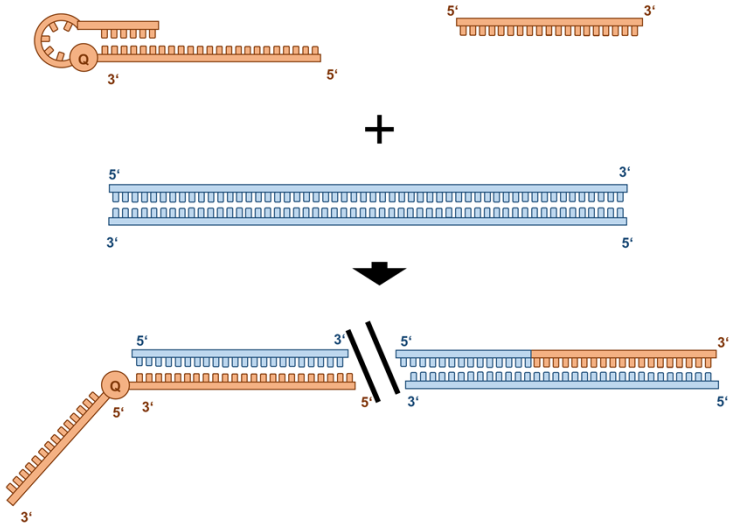

Fig. 3. Isothermal amplification reaction: Specific primer binds to double stranded target sequence, which is accessible due to DNA associated proteins. In the next step an isothermal Polymerase elongates the primer and generates with each amplicon a product with a ssDNA tail. This ssDNA tail is reverse complementary to the capture molecule immobilized on the glass surface. The amplification reaction is continued until one of the reaction components is imitating.

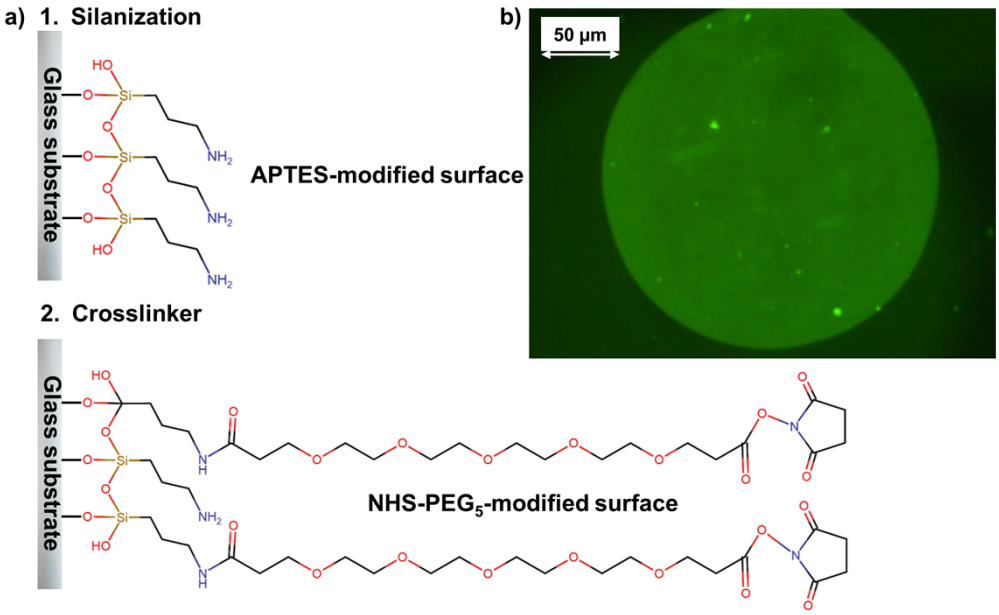

Fig. 4. (a) Schematic of the APTES-modified glass surface functionalization with bis-NHS-PEG_5 crosslinker for coupling proteins on the NHS ester terminals; (b) Resulting photograph of a spot with fluorescence (6-FAM)-labeled ssDNA tails.

Biomedical Optics EXPRESS

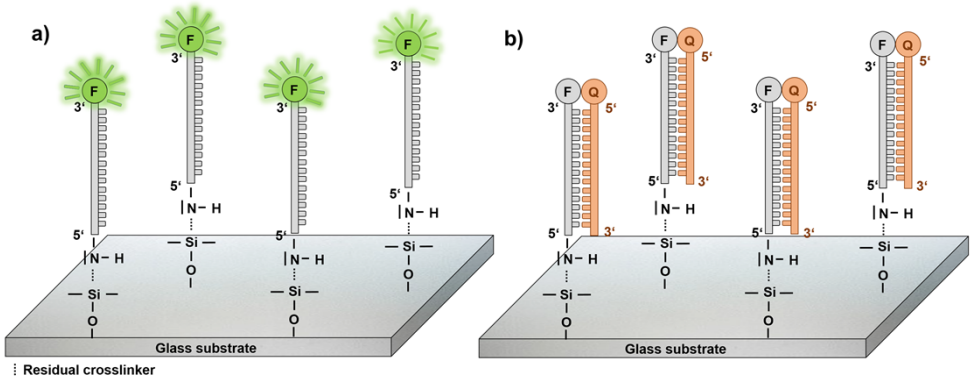

Fig. 5. a) Schematic of immobilized capture molecules; b) Binding of ssDNA tail of target amplicon to immobilized capture molecule and the resulting fluorescence quenching.

2.4. OLED-OPD detection unit fabrication and device characterization

Figures 6(a,b,d) show the organic stacks, a geometrical schematic and a photograph of the test chip with 8 OLED-OPD detection units. The realized TCTA:FIrPic OLEDs and DMQA:DCV3T OPDs are fabricated on a 25 mm × 25 mm glass substrate with a thickness of 1 mm. Each substrate contains 4 test chips, which are separated afterwards to 12.5 mm × 12.5 mm sensing units by a wafer saw. Here, each test chip has 8 OLED-OPD detection units with each device size of 0.5 mm * 0.5 mm. The blue emitting OLED (peaking at ~468 nm and ~494 nm) pixels fabrication was carried out on indium-doped tin oxide (ITO) covered glass by thermally evaporating organic materials. The ITO layer was structured via ultraviolet (UV) photolithography and wet etching to form the 130 nm thin anodes. The organic layers, in sequence, are the hole transport layer of 5 nm molybdenum trioxide (MoO3) and 35 nm 1,1-bis[(di-4-tolylamino)phenyl]cyclohexane (TAPC), then for the emission layer a 20 nm of tris(4-carbazoyl-9-ylphenyl)amine (TCTA) doped with 8% Bis[2-(4,6-difluorophenyl)pyridinato-C2,N](picolinato)iridium (FIrPic) to fabricate a blue emitting OLED. As the electron transport layer (ETL) and hole blocking layer (HBL) a film of 50 nm 2,2',2''-(1,3,5-Benzinetriyl)-tris(1-phenyl-1-H-benzimidazole) (TPBi) is deposited followed by the cathode pads consisting of 1 nm lithium fluoride (LiF) and 175 nm aluminum (Al). Consequently, the OLED pixels are defined by the overlapping regions of mutually perpendicular ITO and Al pads. The OPD structure starts with 30 nm molybdenum trioxide (MoO_3) layer deposited on the indium-tin-oxide (ITO) coated glass. The organic bilayer structure is composed of 30 nm N,N-Dimethyl quinacridone (DMQA) as the common donor and 30 nm 3',4'-Dibutyl-5,5''-bis(dicyanovinyl)-2,2':5',2''-terthiophene (DCV3T) as the acceptor layer. Next, 8 nm 2,2',2''-(1,3,5-Benzinetriyl)-tris(1-phenyl-1-H-benzimidazole) (TPBi) was evaporated followed by 1 nm lithium fluoride (LiF) and 175 nm aluminum (Al) to form the cathode pads. The fabricated devices were encapsulated in a nitrogen-filled glovebox to prevent degradation of the organic layers upon measurements outside the glovebox [16]. Figure 6(c) shows the normalized photoluminescence spectrum of the OLED, with an excitation wavelength peaks at 468 nm and 494 nm, the spectrum of the OPD with the DMQA:DCV3T absorptive bilayer and the spectra of the 6-FAM dye with an excitation and emission wavelength of approx. 496 nm and 521 nm, respectively. The electrical characterization of the OPD is shown in Fig. 6(e). We performed the current-voltage measurement sweep by a source measure unit (SourceMeter 2450, Keithley Instruments, USA) while illuminating the device with a collimated laser module (CPS520, 4.5 mW, Thorlabs GmbH, Lübeck, Germany). The OPD displays a typical diode characteristic with a good sensitivity. The darkcurrent density at 0 V was determined as 15 nA/cm^2 and approx. 0.7 mA/cm^2 are obtained for an incident light power of approx. 0.8 mW/cm^2.

Biomedical Optics EXPRESS

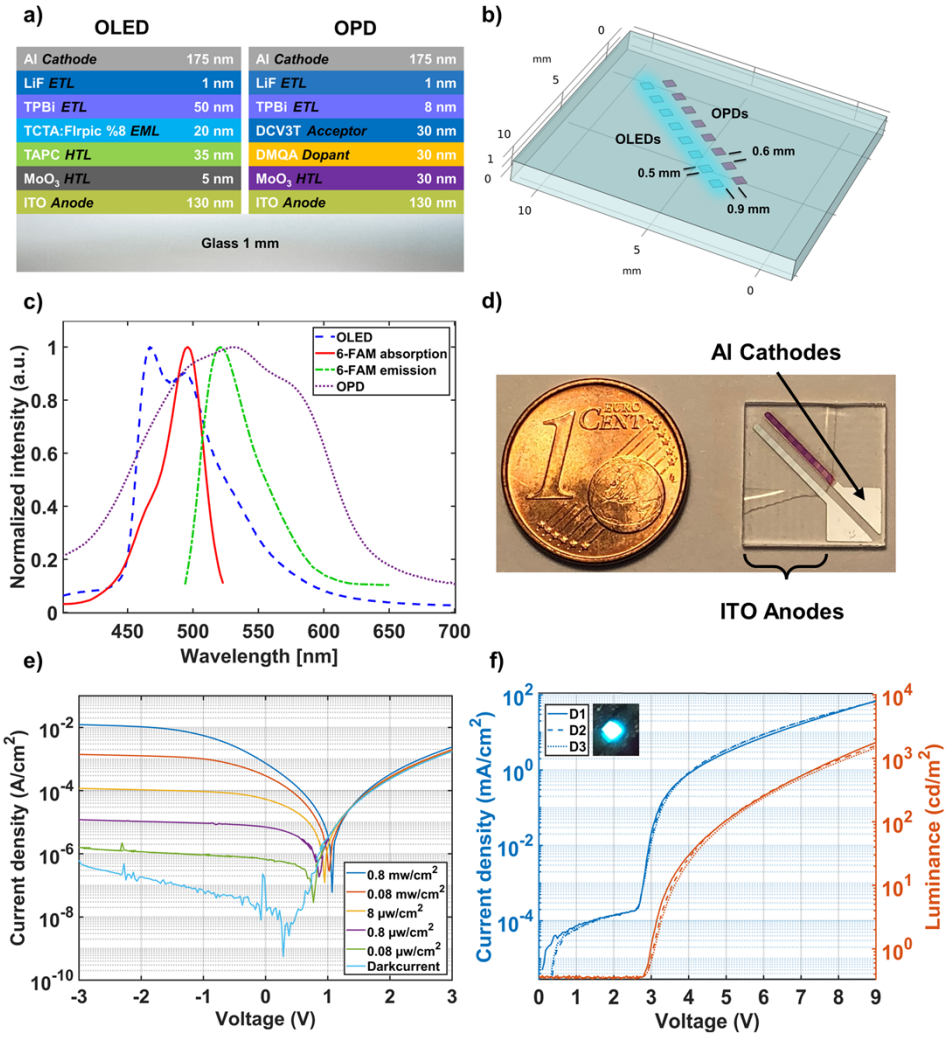

Fig. 6. Fabrication of the OLED-OPD unit for fluorescence sensing. (a) Schematic diagram of the OLED and OPD stacks on a single glass substrate; (b) Geometrical model of the OLED–OPD unit layout with 8 pixel pairs on one test chip; (c) Normalized absorption and emission of 6-FAM [23] and the spectral characteristics of 8 wt% FIrPic in TCTA host OLED emission and the DMQA:DCV3T OPD absorption; (d) Photograph of the fabricated test chip; (e) Current density-voltage characteristics under illumination with a subsequently filtered 520 nm laser and the darkcurrent of the DMQA:DCV3T OPD as an example; (f) J-V-L characteristics of 3 different devices (D1, D2 and D3) as an example.

Biomedical Optics EXPRESS

The OLED was characterized using a commercial calibrated Si-photodiode (FDS1010 Cal, Thorlabs GmbH, Lübeck, Germany) and two source measure units (SourceMeter 2450 & 2400, Keithley Instruments, Cleveland, USA). We placed the light source on top of the large-area photodiode and collected the outcoupled light. Hence, we calculated the current density and the luminance (Fig. 6(f)) with the recorded OLED current and the photocurrent induced by the OLED. We performed all further calculations considering the whole OLED spectrum by multiplying the sensitivity curve of the calibrated Si-PD with the normalized OLED spectrum and the subsequent integration of the relevant wavelength. The onset voltage is approximately 3 V. The measurement was performed with 3 different devices in sequence and shows a good reproducibility. The inset shows a photograph of the 0.5 mm * 0.5 mm OLED pixel operated at 9 V. Here we achieved a luminance of ~1700 cd/m^2 and a current density of 70 mA/cm^2 at 9 V. Additionally, we obtained a maximum current efficiency η of 2.7 cd/A. Due to our observation of a damage threshold voltage between 10 V and 12 V for our devices, we decided to apply 9 V as the operation voltage.

3. Fluorescence sensing setups for ssDNA detection

3.1. 6-FAM-labeled ssDNA characterization on a fluorescence microscope

As the first step towards a compact fluorescence sensing setup we started our experiments with a characterization of our samples on a fluorescence microscope. In this study we evaluated the feasibility of immobilization of capture molecules by measuring the fluorescence after application and washing. Subsequently, we added the ssDNA hosting a quencher, to simulate whether this part of the target amplicon would fit to the capture molecule. In case of a successful binding 6-FAM and the quencher BHQ1 will undergo FRET. Consequently, we expect a suppression of fluorescence.

Figure 7 shows a verification photograph and the spectra of 6-FAM labeled ssDNA spots on a glass substrate after successful binding of fluorescence-labeled ssDNA. We used a spotter (Nanoplotter 2.0, GeSiM Gesellschaft für Silizium-Mikrosysteme mbH, Germany) to fabricate 9 homogeneous spots with each diameter of 200 µm and 200 µm space between the single spots (Fig. 7(a)). Figure 7(b) shows the spectra of 6 randomly picked spots across one fabrication batch. The shape of the spots is highly homogeneous, whereas the fluorescence intensity varies up to a factor of 2. The variability could be further reduced by optimization of the surface functionalization. However, here our aim is to analyze the measurement system aspects and the functionalization is not studied further. As a verification of the hybridization sensing mechanism we investigated the behavior of one single 6-FAM-labeled ssDNA spot, as shown in Fig. 7(c). Here, we took one picture before and one after the application of the complementary BHQ-labeled ssDNA strand in TE buffer as a drop. The second picture shows a successfully quenched area with a fully suppressed fluorescence spot at the location of the applied quencher drop. Thus, this results show readiness off the assay for detecting EHV on a fluorescence microscope.

3.2. Laser excitation of 6-FAM-labeled ssDNA and detection on OPD

Towards a compact fluorescence measurement system we implemented in the first step a laser and OPD based setup, as depicted in the schematic of Fig. 8(a). The 6-FAM-labeled ssDNA sample was diluted in TE buffer solution. We used DNase, DNA and RNase free micro cuvettes as sample holder. We chose a 488 nm laser diode (BLD-488-58, Lasertack GmbH, Germany) as the light source, a collimating lens and a 480 nm bandpass filter on the excitation side. On the detection side we implemented a DMQA:DCV3T OPD with a preceding lens and a 527 nm bandpass filter to avoid the excitation light reaching the detector. Additionally, we used a dichroic mirror for splitting of the excitation light and the fluorescence and performed the experiments in a dark environment.

Biomedical Optics EXPRESS

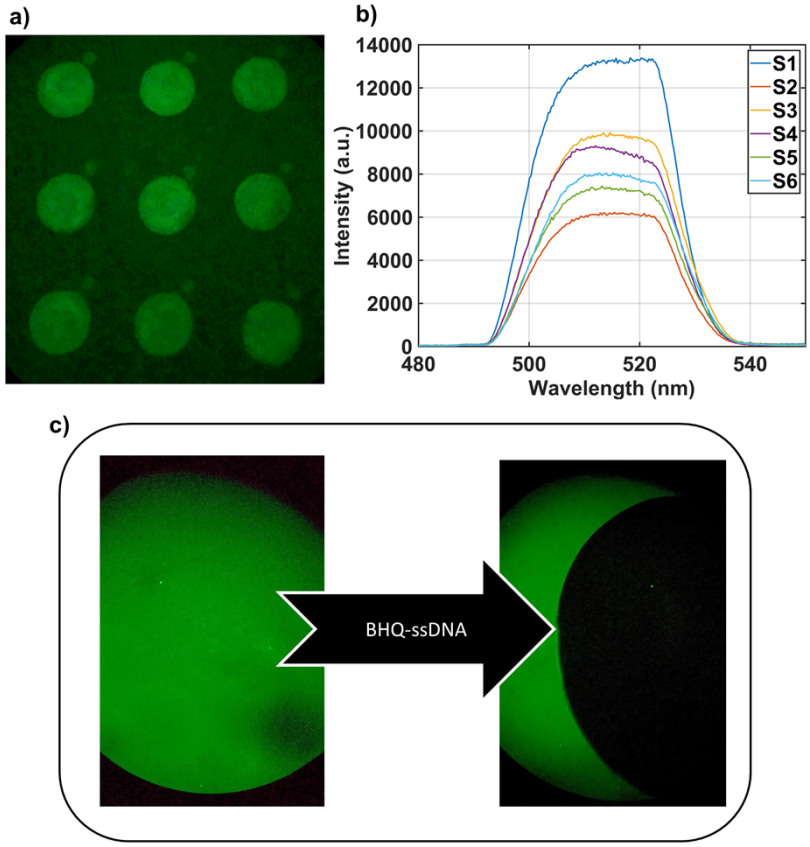

Fig. 7. (a) Photograph of 9 6-FAM-labeled ssDNA spots with each spot diameter of approx. 200 µm made on a fluorescence microscope; (b) Spectral characteristic of 6 random chosen spots as an example; (c) Photograph of a 6-FAM-labeled ssDNA spot, before and after applying a BHQ drop. After the hybridization to dsDNA the FRET based quenching process can clearly be observed by forming a dark spot as seen in the right picture.

Figure 8(b) shows a photograph of the investigated labeled ssDNA samples. The left cuvette contains the 6-FAM-labeled ssDNA, which shows the characteristically green emission of the fluorescent molecules. The right cuvette contains a 50/50 (wt/wt) mixture of 6-FAM-labeled ssDNA and the complementary BHQ-labeled ssDNA, both in 8.45 µM. As expected FRET was successfully observed even with the naked eye. The fluorescence gets suppressed after the hybridization to dsDNA and the resulting proximity of the 6-FAM and BHQ molecules. In the next step we evaluated the sensing performance of our laser diode and OPD based measurement setup. Figure 8(c) shows the fluorescence measurement, starting with 5 premixed fluorescein standard samples in cuvettes ranging from 2 mg/l to 10 mg/l. We illuminated every sample for 40 s and recorded the photocurrent on the OPD. The signal peak at the beginning of each sample is based on diffuse reflection of the laser light due to the manual change of the cuvettes and can be neglected. The observed increase of the photocurrent upon the increase of the fluorescein concentration is shown for the first 5 samples. Furthermore, we also observed a strong photo bleaching of the fluorescein, due to the illumination of the sample with the laser. Hence, we obtained the calibration function by taking the last measurement point for each fluorescein standard signal. We calculated the sensitivity as $S = 1$ nA/(mg/l) offering a linearity of approx. 99%. The standard deviation of the current noise level is determined as $\sigma = 21$ pA. This yields

Biomedical Optics EXPRESS

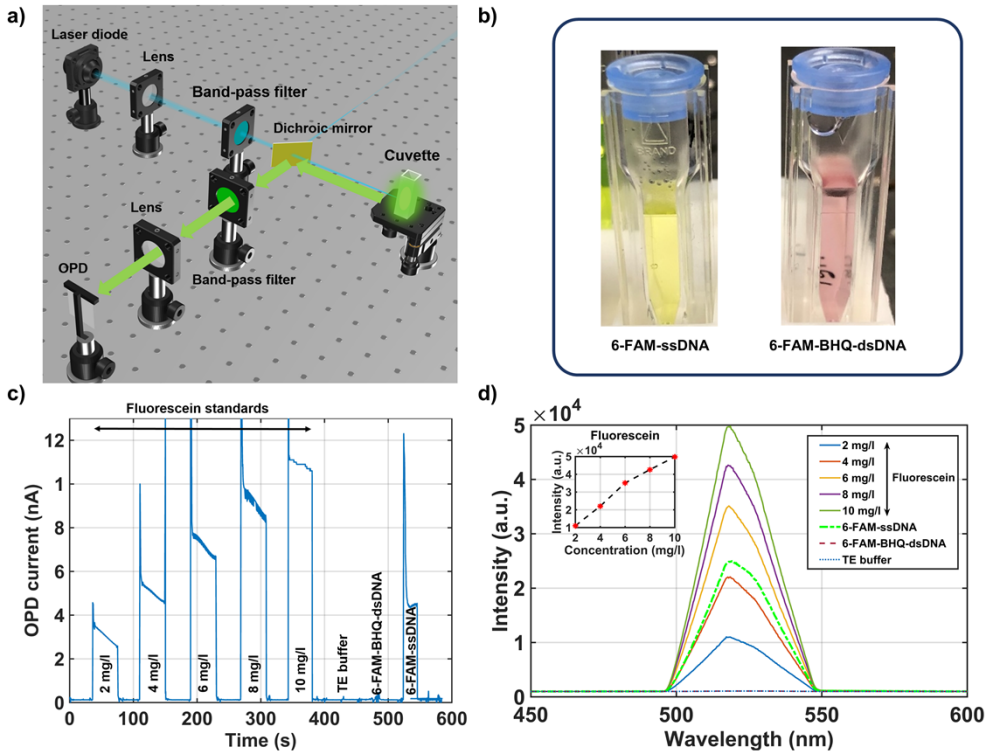

Fig. 8. (a) Schematic diagram of the fluorescence sensing setup based on a laser diode as the excitation source and an OPD as detector; (b) Photography of 6-FAM labeled ssDNA sample diluted in TE buffer (left) and a 6-FAM labeled ssDNA sample mixed with the complementary BHQ1 labeled ssDNA quencher system; (c) Fluorescence measurement of premixed fluorescein standards and bio-samples; (d) Spectral characteristics of the measured samples. The inset shows a linear behavior of the fluorescein standards.

a limit of detection (LOD) of LOD = 3×σ/S = 63 µg/l (150 nM). Next, we proceeded with the DNA hybridization measurements. As shown in Fig. 8(c) we recorded in the last 3 measurements subsequently the resulting OPD photocurrent of a cuvette with TE buffer, a cuvette with a 50/50 (wt/wt) mixture of 6-FAM-labeled ssDNA and the BHQ-labeled ssDNA (as depicted in Fig. 8(b) right) and a cuvette of the 6-FAM-labeled ssDNA. The concentration of the ssDNA samples was always fixed at 8.45 µM. This measurement also confirms that the hybridization of the ssDNA strands to dsDNA takes place with subsequent FRET based fluorescence quenching. Furthermore, we excluded any influence of the laser induced light on the OPD by testing the clear TE buffer sample. This reference measurement is seen in Fig. 8(c) at around 420 s. No signal is observed on the OPD. Thus, the combination of the excitation and emission filters with the dichroic mirror allows a strong suppression of undesired background signal in the measurements. As a verification of the measurements we checked the spectral characteristics of the investigated samples prior to the laser measurements. As depicted in Fig. 8(d) the fluorescein standard solutions and the 6-FAM-labeled ssDNA show the expected emission peak at approx. 520 nm. The quenched sample and the TE buffer show no fluorescence intensity. These results show that using a laser diode and an OPD has a high potential to be employed in compact systems for DNA hybridization measurements. However the process of integrating a laser diode and an OPD as a LOC system cannot easily be upscaled for parallel fabrication of many sensor units. Thus,

Biomedical Optics EXPRESS

we investigate DNA hybridization sensing on a full organic optoelectronic chip with in-plane integrated devices in the following chapter.

3.3. Fluorescence sensing with the OLED-OPD detection unit

As the next step towards POC testing we used our OLED-OPD chip for fluorescence sensing. Figure 9(b) shows an exploded-view schematic of the detection setup. We contacted the OLED-OPD chip (Fig. 6(b,d)) with elastomeric ZEBRA connectors, using a printed circuit board (PCB) with mirrored electrodes design. The OLED-OPD chip and the PCB are pressed with caps and the housing to ensure electrical contact and prevent displacement. The fluid chamber is sealed with a rubber seal (9.5 mm by 9.5 mm by 3 mm) to ensure tightness and avoid leakage of the liquid samples resulting in a volume of approx. 270 µl. Two butterfly cannulas were used to form the in- and outlets. They are punched through the rubber into the chamber. Figure 9(c) shows a photograph of the setup. The measurements were performed with two source-measure units (SMUs) for OLED power supply and recording the photocurrent of the OPD. To characterize the system we performed a fluorescence measurement with a dilution series of fluorescein again ranging from 2 mg/l to 10 mg/l. Figure 9(a) shows the OPD photocurrent as a function of dye concentrations. Every 100 s we changed the analyte to investigate the photocurrent change between DI water and the increasing fluorescein concentration. The inset of the plot shows the background corrected staircase shaped increasing signal, due to the increased fluorescence signal. For example, the absolute photocurrent changed to 0.18 nA after addition of a 10 mg/l fluorescein standard solution. The calibration function obtained from these measurements was found to be linear within the tested region, offering linearity of approximately 99%. The sensitivity was calculated as S = 10 pA/(mg/l). The standard deviation current noise level was determined as $\sigma = 3$ pA. This yielded a limit of detection (LOD) of $LOD = 3 \times \sigma/S = 0.7$ mg/l (1.7 µM). Pais et al. [12] reported a transmission based setup with an OLED and an OPD fabricated on separate substrates and two orthogonally orientated polarizers to filter out the excitation light. They obtained an LOD of 10 µM for fluorescein, which shows that our OLED-OPD unit already show a better performance by approx. a factor of 6. Finally, we proceeded with the ssDNA hybridization sensing. In Fig. 9(d) we show the fluorescence signal under OLED excitation of 6-FAM-ssDNA and premixed 6-FAM-BHQ-dsDNA with fixed concentrations at 8.45 µM. The inset of the figure shows the original data with the typical degradation behavior of the OLED. For 6-FAM-ssDNA the OPD photocurrent increases due to the fluorescence of 6-FAM and drops for approx. 0.14 nA after flushing the chamber with the premixed 6-FAM-BHQ dsDNA. Figure 9(d) shows the background corrected measurement.

These results show successful DNA hybridization sensing on a fully organic-semiconductor-based in-plane integrated sensor. We believe that this OLED-OPD detection unit is a highly relevant first step towards the realization of compact, low-power point-of-care devices in the veterinary or human diagnostic.

Our long-term goal is the realization of multiplexed detection by specific binding of fluorescence-labeled biomaterial. For example, our OLED-OPD chip design with 8 OLED-OPD pairs is a suitable POC system for testing of four different biomarkers with a reference site each. By local functionalization this would allow eight simultaneous measurements on one single chip without the need for wavelength multiplexing. To test this idea, we prepared a series of glass slides with immobilized 6-FAM-ssDNA strands as capture molecules as shown in Fig. 7(a). The goal was to excite the 6-FAM-ssDNA spots with the OLEDs and measure the FRET after adding BHQ-ssDNA. In this set of experiments, the OLED-OPD detection unit showed no signal change after applying a BHQ-labeled ssDNA drop even though the fluorescence microscope showed clear and successful binding of 6-FAM-ssDNA on the glass slides. The fluorescence emission of the 6-FAM-labeled monolayer of surface bound capture molecules provide weaker fluorescence signal, due to the smaller absolute amount of fluorophores inside the fluidic chamber compared to

Biomedical Optics EXPRESS

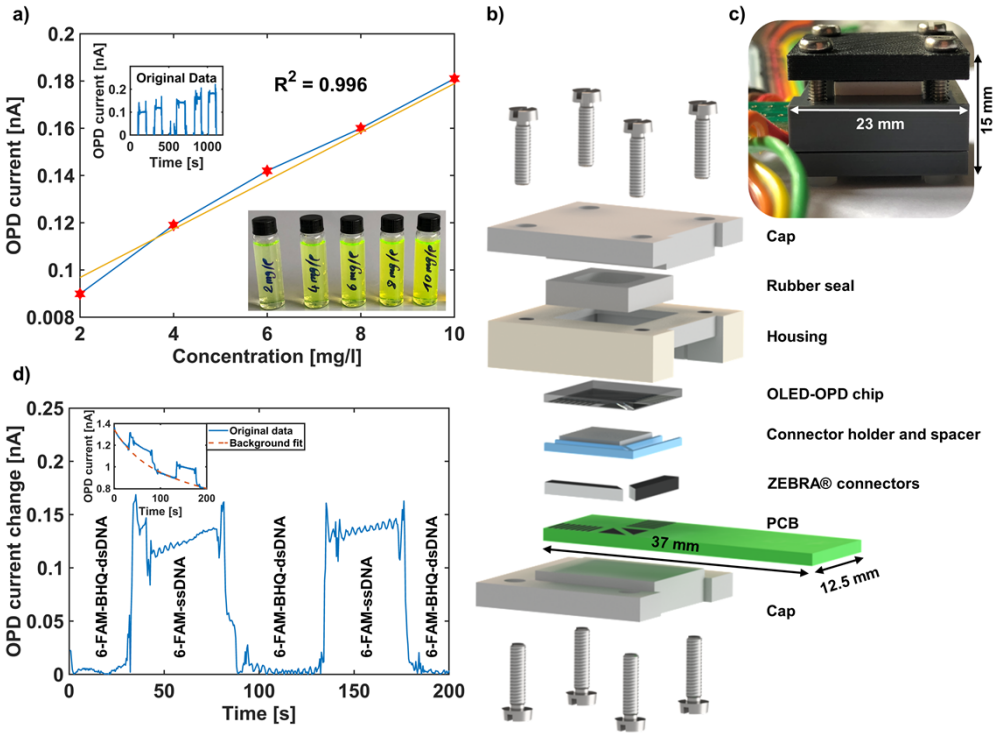

Fig. 9. (a) Photoresponse of the OPD for the dilution series of fluorescein dye with OLED excitation. The inset shows the original data and the main plot represents the amount of photocurrent induced on the corresponding fluorescein concentration; (b) Exploded-view drawing of the detection setup. The OLED-OPD chip is contacted with elastomeric ZEBRA connectors, using a printed circuit board (PCB) with mirrored electrodes design. The OLED-OPD chip and the PCB are pressed with a cap and the housing to ensure electrical contact and prevent displacement. The fluid chamber is sealed with a rubber seal; (c) Photograph of the detection unit; (d) Fluorescence measurement of the 6-FAM-ssDNA and the hybridized 6-FAM-BHQ-dsDNA samples as liquids with fixed concentration at 8.45 µM. The inset shows the original data and the typical degradation of the OLED during the operation.

Biomedical Optics EXPRESS

the measurement with higher concentrated liquid samples. Thus, the signal-to-noise ratio of our OLED-OPD detection unit is not sufficient yet for detection of immobilized DNA hybridization sensing. In the next chapter we investigate the system efficiency in order to give a feasibility analysis.

3.4. System efficiency and light budget of the OLED-OPD detection unit

3.4.1. Raytracing simulations

To evaluate the current system efficiency we conducted ray tracing simulations with the Ray Optics Module in COMSOL Multiphysics. In the first simulation we investigate the efficiency of the 6-FAM-ssDNA spot excitation by the OLED. We assume that the OLED releases the emission power with a Lambertian emission pattern directly from the semitransparent ITO anode layer, which gets partly absorbed by the fluorescence dye spot modeled as a ray detector. The wavelength was fixed at 495 nm, since our hybridization sensing assay was developed based on 6-FAM as the fluorescence dye. We located the spot above the OPD in our model (Fig. 10(a,b)) with the same size of active region as the photodetector to achieve the highest fluorescence intensity upon a successful excitation of the fluorescence spot. As the total OLED emission power we obtained $J_{OLED} = 3.5$ mW/cm^2 (active area of 0.25 mm^2 as reference) operating the OLED at 9 V and using a calibrated Si-PD and considered this value in our simulations. Finally, the excitation power on the spot was simulated as $E_{SPOT} = 95$ µW/cm^2. We calculate that only $\eta_{Ill} = 2.7\%$ of initial OLED emission power reach the fluorescence spot, which is due to the small solid angle of the fluorescence spot as viewed from the OLED. Figure 10(b) shows a sideview of a simulation snapshot with our OLED-OPD model. Most of the OLED light does not reach the fluorescence spot.

In the next simulation step, we consider how much fluorescence emission reaches the OPD. To estimate the initial fluorescence emission power we prepared a glass slide fully covered with surface bound 6-FAM-ssDNA and measured the transmission spectrum with a UV-Vis spectrometer (Lambda 800, PerkinElmer, USA). The absorption around 496 nm was measured to be approx. $\eta_{Abs} = 3\%$. Additionally, we considered the quantum yield of $\eta_{QY} = 95\%$ for fluorescein [24] and calculated the energy conversion efficiency of $\eta_{\Delta E} = \lambda_{Ex}/\lambda_{Em} = 95.2\%$ due to the wavelength shift from 496 nm to 521 nm. Considering all factors leads to a total fluorescence efficiency at the spot of $\eta_{Fl} = \eta_{Abs} * \eta_{QY} * \eta_{\Delta E} = 2.7\%$. Thus, we defined the fluorescence spot in the next step of our simulation as a spherical ray release device (Fig. 10(a)) with a source emission power of $J_{SPOT} = E_{SPOT} * \eta_{Fl} = 2.6$ µW/cm^2. Due to the small solid angle, the OPD detected approx. $\eta_{Det} = 1.8\%$ of the initial released rays resulting in an OPD irradiance of $E_{OPD} = J_{SPOT} * \eta_{Det} = 46$ nW/cm^2. According to our simulations the system efficiency of the OLED emission power to OPD irradiance with the fluorescence emission of the dye spot is calculated to be approx. $\eta_{Sys} = E_{OPD} / J_{OLED} = 0.013‰$. The simulation results are summarized in Table 1.

Table 1. System Efficiency Simulation

Simulation Benchmarks	Determination	Efficiency Factor	Value
OLED emission power density J_{OLED}	Measured	-	3.5 mW/cm^2
6-FAM-ssDNA spot illumination E_{SPOT}	Simulated	$\eta_{Ill} = E_{SPOT} / J_{OLED}$	95 µW/cm^2
6-FAM-ssDNA emission power density J_{SPOT}	$E_{SPOT} * \eta_{Fl}$	$\eta_{Fl} = \eta_{Abs} * \eta_{QY} * \eta_{\Delta E}$	2.6 µW/cm^2
Fluorescence radiation on OPD E_{OPD}	Simulated	$\eta_{Det} = E_{OPD} / J_{SPOT}$	46 nW/cm^2
System efficiency	E_{OPD}/J_{OLED}	η_{Sys}	0.013‰

As a conclusion, the simulated low system efficiency of $\eta_{Sys} = 0.013‰$ is attributed to three dominant loss factors – the low irradiation of the 6-FAM-ssDNA spot by the OLED, the low irradiation of the OPD by the fluorescence emission of 6-FAM-ssDNA, and the high transmission

Biomedical Optics EXPRESS

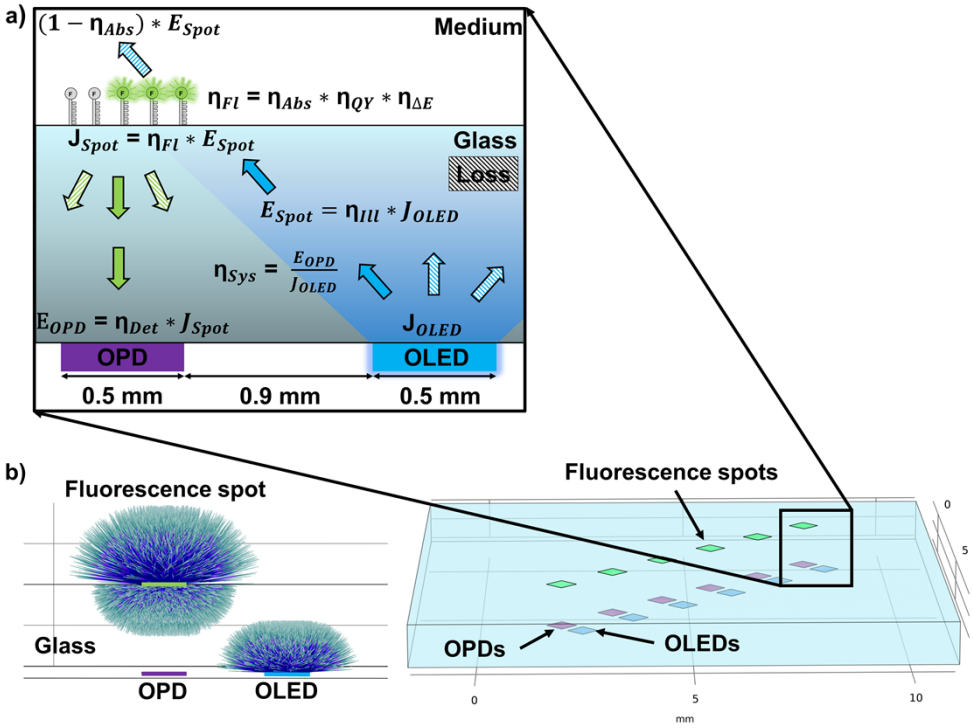

Fig. 10. Ray-Tracing simulation model. (a) 3D view of the full OLED-OPD unit model with 8 pixel pairs on one substrate. The 6-FAM-labeled-ssDNA spots are placed above the OPDs. The zoomed inset shows a 2D schematic, the efficiency factors and the geometrical properties of one OLED-OPD pixel pair and the fluorescence spot; (b) Sideview of an OLED-OPD pair model with a fluorescence spot above the OPD. The OLED was modeled as a Lambertian emitter and the fluorescence spot as a spherical ray release source.

through the monolayer of 6-FAM-ssDNA capture molecules. The first two factors are due to the geometrical losses of the monolithically integrated OLED-OPD system. The geometrical losses are visualized in the Fig. 10(b) as a plot that shows a snapshot of the simulated ray trajectories of one OLED and one fluorescence spot. The picture shows clearly the high fraction of excitation rays, which do not arrive at the fluorophore, and fluorescence rays not reaching the OPD. Thirdly, the monolayer of 6-FAM-ssDNA capture molecules transmits approx. 97% (1-η_{Abs}) of incident light. In Table 2 we summarized all considered loss factors and highlighted the dominant ones, which can be minimized with a manageable effort.

3.4.2. Experimental system light budget

In order to verify dominating system limitations we performed further system characterization experiments. We stress that all power density measurements in this chapter were done with our calibrated Si-photodiode and we referenced all values to the active area of 10 mm by 10 mm for a good comparison. We investigated the noise equivalent power (NEP) of the OPD and evaluated the available fluorescence emission power of a 6-FAM-ssDNA spot to estimate the light budget on the detector side. Here we obtained a NEP of 6.4 nW/cm^2 for our OPD with the 520 nm collimated laser module. The NEP equals the lowest irradiation on the detector for generating a photocurrent above the noise level. The emission power density of the 6-FAM-ssDNA spots were subsequently investigated on the fluorescence microscope. Here we focused the fluorescence

Biomedical Optics EXPRESS

Table 2. Light Budget: Summary of Loss Factors and Improvement Options

Factor	Loss Value	Recommendation
Initial OLED emission power	-	Tuning of organic stacks [25]
Small solid angle of OLED on 6-FAM-ssDNA spot	~97.3%	Use of directional OLEDs, integration of optical elements
6-FAM quantum yield	~5%	-
Stokes shift energy transfer	~4.8%	-
6-FAM-ssDNA spot light transmission	~97%	Place spot in cavity
Spherical fluorescence emission	~98.2%	Reduce the distance between the OPD and the fluorescence spot to collect ~50% of light, integration of optical elements

emission output of one single spot on the Si-Photodiode and calculated an emission power density of approx. 800 nW/cm^2. Thus, the available fluorescence signal under illumination on the microscope lamp is 125 times higher, than the lowest required power density on the OPD to generate a signal above the noise level. Consequently, the detection side of the OLED-OPD unit is evidently not in principle a limitation factor.

As the next step we investigated the efficiency of the 6-FAM-ssDNA excitation with our fabricated FIrPic-OLED. First, we evaluated the excitation intensity under the fluorescence microscope. For our ssDNA assay evaluation experiments (Chapter 3.1) we used the maximum available intensity of the excitation light, which is expected to be much higher than the OLED emission power. Here we placed our Si-Photodiode directly on the stage of our microscope and obtained approx. 15.5 mW/cm^2 as the emission power density. Subsequently we placed again our 6-FAM-ssDNA spot on the stage of the microscope, decreased stepwise the intensity of the excitation light, until the emission spectrum of 6-FAM around 520 nm reached the intensity level of the background signal of the CCD detector. We measured this power density as 60 µW/cm^2 and defined this value as the minimum required emission power density for a successful excitation of the 6-FAM-ssDNA spot. Next, we calculated the emission power density from the OLED normalized to the active area of the Si-PD. For a bias voltage of 9 V the OLED emits 8 µW/cm^2. This power density is 7.5 times lower than the minimum required emission power density for a sufficient excitation of 6-FAM-ssDNA spots and approx. 2000 times lower than the power density of the excitation light used on the fluorescence microscope. Thus, the excitation intensity is currently one of the highest limitation factors for fluorescence sensing of surface bound 6-FAM-ssDNA spots on glass with an OLED-OPD chip.

3.4.3. Discussion

The evaluation above shows that the light budget of the current system is not sufficient to detect with the OPD the fluorescence emission from surface bound 6-FAM-labeled-ssDNA excited by the OLED. To overcome the aforementioned limitations and realize multiplex POC testing further improvements of the system are necessary. Tuning the OLED stacks is a promising next step towards a stable blue emitting FIrPic-OLED with higher damage threshold voltage and thus higher emission power. Liu et al. increased the OLED current efficiency by a factor of ~ 6.5 using a MoO_3 modified ITO as the anode and even by ~ 13.6 by adopting a bilayer device with FIrPic:CBP and FIrPic:TPBi as the double emission layers [25]. We believe, that increasing the efficiency of the OLED will lead to a sufficient excitation for the dye-labeled-ssDNA spots. Additionally, the excitation may also be increased by minimizing the distance between the OLED and the OPD. As an example, reducing the distance from 0.9 mm to 0.1 mm would increase the OLED excitation irradiance on the fluorescence spot by a factor of ~ 1.3 from $\eta_{Det} = 1.8\%$ ($E_{SPOT} = 95$ µW/cm^2) to $\eta_{Det} = 3.95\%$ ($E_{SPOT} = 126$ µW/cm^2). To further improved excitation

Biomedical Optics EXPRESS

performance the integration of planar optical waveguides should be evaluated to get more light on the fluorescence spot. For example, planar waveguides or air mirrors can be directly integrated on microfluidic structures as light guiding elements [26,27]. Furthermore, the geometry of the system should be changed such that the OPD is placed with minimum distance to the fluorescence spots. For this purpose, the optical system could be processed on thin foils. Considering a substrate thickness of 200 µm instead of the current 1-mm glass substrate the simulated efficiency of fluorescence detection could be improved from $\eta_{Det} = 1.8\%$ to $\eta_{Det'} = 22.8\%$. However, this step deserves a careful consideration, since reducing the substrate thickness will lead to a decrease of OLED irradiation on the fluorescence spot. An optimum ratio between the substrate thickness and the OLED-OPD distance has to be evaluated. In summary, the simulations and experiments show that an OLED-OPD detection of surface bound fluorescence markers is within reach with current technology and will profit from the further development of organic optoelectronic devices on thin foils.

4. Conclusions

We investigated a sensing system for decentralized detection of veterinary biomarkers based on an optical detection unit with side-by-side OLED and OPD. This configuration has the advantage of simple assembly and contacting. We developed a specific EHV ssDNA assay based on the hybridization of the fluorescence-labeled ssDNA strand and quencher-labeled reverse complementary ssDNA segments, where the fluorescence of the fluorophore is suppressed upon a certain proximity to the quencher. After the hybridization of the ssDNA segments to dsDNA the fluorophores undergo FRET. We successfully performed the proof-of-concept of hybridization sensing of two complementary dye-labeled ssDNA strands diluted in TE buffer measured on a 12.5 mm by 12.5 mm chip with 8 integrated OLED-OPD pairs. For multiplex POC testing several specific biomarkers of interest can act as capture ssDNA, labeled with different fluorescence molecules. This results in a specific wavelength for a certain biomarker (EHV-1-5 or other viral pathogens), which can be excited and detected with a suitable OLED-OPD pair. An easier approach to multiplex measurements requiring only one type of OLED and one type of OPD is the localized surface binding of a specific biomarker to a specific OLED-OPD detection pair. For this purpose we covalently coupled a fluorescence-labeled ssDNA on a glass surface, which is intended to act as sample capture molecule. We could not detect fluorescence of surface-bound biomarkers with the OLED-OPD chip. We performed a detailed investigation of the limiting factors in the current system. We demonstrated that detection is within reach for improved OLED brightness. Also the system efficiency may be improved employing thinner substrates. This requires at the same time the consideration of directional OLEDs and optical waveguides to achieve efficient fluorescence excitation with the OLED.

The integration of organic optoelectronic devices is a powerful approach pushing further the device sizes towards a highly compact and low-power POC system for biomedical applications. The thermal evaporation technique enables a wide variety of geometrical shapes, sizes and the fabrication on rigid or flexibles substrates. Taking the step towards an in-plane integrated OLED-OPD sensing platform enables the potential for parallel mass fabrication, increasing the commercial viability. Particularly, the fabrication on flexible substrates is highly promising for roll-to-roll fabrication [28]. This monolithic integrated OLED-OPD sensing unit is now ready for biomedical detection of single-type dye-labeled ssDNA in solution.

Funding. European Regional Development Fund (LPW-E/1.2.2/1303, OPTOCHIP); DFG Open Access-Publikationskosten.

Disclosures. NR: altona Diagnostics GmbH (E)

Data availability. Data underlying the results presented in this paper are not publicly available at this time but may be obtained from the authors upon reasonable request.

References

Biomedical Optics EXPRESS

1. C. J. Thieulent, E. S. Hue, C. I. Fortier, P. Dallemagne, S. Zientara, H. Munier-Lehmann, A. Hans, G. D. Fortier, P. H. Pitel, P. O. Vidalain, and S. L. Pronost, "Screening and evaluation of antiviral compounds against Equid alpha-herpesviruses using an impedance-based cellular assay," Virology **526**, 105–116 (2019).
2. G. Perkins, S. Babasyan, A. E. Stout, H. Freer, A. Rollins, C. L. Wimer, and B. Wagner, "Intranasal IgG4/7 antibody responses protect horses against equid herpesvirus-1 (EHV-1) infection including nasal virus shedding and cell-associated viremia," Virology **531**, 219–232 (2019).
3. S. B. Hussey, R. Clark, K. F. Lunn, C. Breathnach, G. Soboll, J. M. Whalley, and D. P. Lunn, "Detection and quantification of equine herpesvirus-1 viremia and nasal shedding by real-time polymerase chain reaction," J. Vet. Diagnostic Investig. **18**(4), 335–342 (2006).
4. P. Daly and S. Doyle, "The development of a competitive PCR-ELISA for the detection of equine herpesvirus-1," J. Virol. Methods **107**(2), 237–244 (2003).
5. H. Lee, E. Kim, Y. Lee, H. Kim, J. Lee, M. Kim, H. J. Yoo, and S. Yoo, "Toward all-day wearable health monitoring: An ultralow-power, reflective organic pulse oximetry sensing patch," Sci. Adv. **4**(11), 1–9 (2018).
6. Y. Khan, D. Han, A. Pierre, J. Ting, X. Wang, C. M. Lochner, G. Bovo, N. Yaacobi-Gross, C. Newsome, R. Wilson, and A. C. Arias, "A flexible organic reflectance oximeter array," Proc. Natl. Acad. Sci. U. S. A. **115**(47), E11015 (2018).
7. E. L. Ratcliff, P. A. Veneman, A. Simmonds, B. Zacher, D. Huebner, S. S. Saavedra, and N. R. Armstrong, "A planar, chip-based, dual-beam refractometer using an integrated organic light-emitting diode (OLED) light source and organic photovoltaic (OPV) detectors," Anal. Chem. **82**(7), 2734–2742 (2010).
8. C. M. Lochner, Y. Khan, A. Pierre, and A. C. Arias, "All-organic optoelectronic sensor for pulse oximetry," Nat. Commun. **5**(1), 5745 (2014).
9. E. Manna, T. Xiao, J. Shinar, and R. Shinar, "Organic photodetectors in analytical applications," Electron. **4**(3), 688–722 (2015).
10. C. Murawski and M. C. Gather, "Emerging biomedical applications of organic light-emitting diodes," Adv. Opt. Mater. **9**(14), 2100269 (2021).
11. T. Mayr, T. Abel, E. Kraker, S. Köstler, A. Haase, C. Konrad, M. Tscherner, and B. Lamprecht, "An optical sensor array on a flexible substrate with integrated organic opto-electric devices," Procedia Engineering **5**, 1005 (2010).
12. A. Pais, A. Banerjee, D. Klotzkin, and I. Papautsky, "High-sensitivity, disposable lab-on-a-chip with thin-film organic electronics for fluorescence detection," Lab Chip **8**(5), 794–800 (2008).
13. R. Liu, T. Xiao, W. Cui, J. Shinar, and R. Shinar, "Multiple approaches for enhancing all-organic electronics photoluminescent sensors: simultaneous oxygen and pH monitoring," Anal. Chim. Acta **778**, 70–78 (2013).
14. C. Lian, K. Yoshida, C. Nogues, and I. D. W. Samuel, "Organic light-emitting diode based fluorescence sensing system for DNA detection," Adv. Mater. Technol. **7**(5), 2100806 (2022).
15. I. Titov, M. Köpke, N. Schneidewind, J. Buhl, Y. Murat, and M. Gerken, "OLED OPD matrix for sensing on a single flexible substrate," IEEE Sens. J. **20**(14), 7540–7547 (2020).
16. I. Titov, M. Köpke, and M. Gerken, "Monolithic integrated OLED–OPD unit for point-of-need nitrite sensing," Sensors **22**(3), 910 (2022).
17. R. Abbel, I. De Vries, A. Langen, G. Kirchner, H. T'Mannetje, H. Gorter, J. Wilson, and P. Groen, "Toward high volume solution based roll-to-roll processing of OLEDs," J. Mater. Res. **32**(12), 2219–2229 (2017).
18. N. Sun, C. Jiang, Q. Li, D. Tan, S. Bi, and J. Song, "Performance of OLED under mechanical strain: a review," J. Mater. Sci.: Mater. Electron. **31**(23), 20688–20729 (2020).
19. L. Le Reste, J. Hohlbein, K. Gryte, and A. N. Kapanidis, "Characterization of dark quencher chromophores as nonfluorescent acceptors for single-molecule FRET," Biophys. J. **102**(11), 2658–2668 (2012).
20. C. Wang, C. Y. Lim, E. Choi, Y. Park, and J. Park, "Highly sensitive user friendly thrombin detection using emission light guidance from quantum dots-aptamer beacons in 3-dimensional photonic crystal," Sens. Actuators, B **223**, 372–378 (2016).
21. M. Gilar, K. J. Fountain, Y. Budman, U. D. Neue, K. R. Yardley, P. D. Rainville, R. J. Russell, and J. C. Gebler, "Ion-pair reversed-phase high-performance liquid chromatography analysis of oligonucleotides: Retention prediction," J. Chromatogr. A **958**(1-2), 167–182 (2002).
22. G. T. Hermanson, Bioconjugate Techniques Chapter 18 - PEGylation and Synthetic Polymer Modification (2013).
23. T. J. Lambert, "FPbase: a community-editable fluorescent protein database," Nat. Methods **16**(4), 277–278 (2019).
24. J.R. Lakowicz, *Principles of Fluorescence Spectroscopy*, 2nd Ed., (Kluwer Academic/Plenum Publishers, 1999).
25. Z. Liu, M. G. Helander, Z. Wang, and Z. Lu, "Band alignment at anode/organic interfaces for highly efficient simplified blue-emitting organic light-emitting diodes," J. Phys. Chem. C **114**(39), 16746–16749 (2010).
26. S. Balslev, A. M. Jorgensen, B. Bilenberg, K. B. Mogensen, D. Snakenborg, O. Geschke, J. P. Kutter, and A. Kristensen, "Lab-on-a-chip with integrated optical transducers," Lab Chip **6**(2), 213–217 (2006).
27. A. Llobera, S. Demming, R. Wilke, and S. Büttgenbach, "Multiple internal reflection poly(dimethylsiloxane) systems for optical sensing," Lab Chip **7**(11), 1560–1566 (2007).
28. Y. Murat, K. Petersons, D. Lanka, L. Lindvold, L. Yde, J. Stensborg, and M. Gerken, "All solution-processed ITO free flexible organic light-emitting diodes," Mater. Adv. **1**(8), 2755–2762 (2020).